NASA TECHNICAL NOTE

NASA TN D-4172

NASA TN D-4172

GASEOUS-HYDROGEN - LIQUID-OXYGEN ROCKET COMBUSTION AT SUPERCRITICAL CHAMBER PRESSURES

by Martin Hersch and Edward J. Rice

Lewis Research Center

Cleveland, Ohio

NATIONAL AERONAUTICS AND SPACE ADMINISTRATION • WASHINGTON, D. C. • SEPTEMBER 1967

NASA TN D-4172

GASEOUS-HYDROGEN - LIQUID-OXYGEN ROCKET COMBUSTION AT SUPERCRITICAL CHAMBER PRESSURES

By Martin Hersch and Edward J. Rice

Lewis Research Center
Cleveland, Ohio

NATIONAL AERONAUTICS AND SPACE ADMINISTRATION

For sale by the Clearinghouse for Federal Scientific and Technical Information
Springfield, Virginia 22151 – CFSTI price $3.00

GASEOUS-HYDROGEN - LIQUID-OXYGEN ROCKET COMBUSTION AT SUPERCRITICAL CHAMBER PRESSURES

by Martin Hersch and Edward J. Rice

Lewis Research Center

SUMMARY

The effect of wide variations in chamber pressure on rocket combustor performance was determined for the gaseous-hydrogen - liquid oxygen propellant system. A series of combustors with two different contraction ratios, 2, and 10, was used to cover a nominal chamber pressure range of approximately 300 to 1800 psia (2.06×10^6 to 1.24×10^7 N/m^2 absolute) at a thrust range of 100 to 200 pounds force (444 to 888 N). The nominal oxidant-fuel mixture ratio was 2.3, which is that required for maximum theoretical characteristic exhaust velocity. Chamber length was varied from 2 to 10 inches (5.08 to 25.4 cm) at each pressure level. The chamber pressure was increased by increasing the propellant flow rate and by decreasing the nozzle throat area at a constant contraction ratio.

Performance efficiencies for the combustor with a low contraction ratio increased with increasing chamber pressure, while those combustors with a high contraction ratio decreased with increasing chamber pressure. These apparently contradictory results were explained by using both an experimental drop size correlation that indicates drop size increases with increasing chamber pressure and a vaporization model with flash vaporization in the nozzle.

The analysis of the contradictory results indicated that the calculated characteristic exhaust velocity C* performance based on the static chamber pressure can exceed 100 percent. This performance is possible because of the large total pressure loss that occurs with burning in the nozzle near the throat.

INTRODUCTION

As the need for higher thrust rocket vehicles increases, it becomes even more desirable to obtain a high ratio of thrust or energy release to rocket-combustion-chamber

volume, which may be accomplished by increasing the combustor chamber pressure.

One hindrance in the design of high-pressure combustors is the lack of controlled experimental performance data over a wide pressure range. It would thus be desirable if experimental performance characteristics were known for a single type of combustor for both low-pressure regions where ample experimental and analytical results are available (refs. 1 to 4) and high-pressure regions where only limited information is available (ref. 5). The purpose, therefore, of the present study is to investigate experimental performance over a wide range of chamber pressures with varying contraction ratios, propellant flow rates (at a constant mixture ratio), nozzle throat diameters, and chamber lengths. These data are compared with available analytical results.

SYMBOLS

A	cross-sectional area, in.^{2}; cm^2
ε	chamber contraction ratio, chamber area/throat area
C^*	characteristic exhaust velocity, $g_c A_t P_c/(W_o + W_f)$ ft/sec; m/sec
C_1, C_2, C_3	constants
D_c	chamber diameter, in.; cm
D_j	diameter of liquid jet, in.; cm
D_m	mass median drop diameter, μm
D_{mc}	D_m correlated (appendix B), μm
D_{mi}	D_m calculated to satisfy vaporization model (ref. 4), μm
D_t	nozzle throat diameter, in.; cm
F	fraction of liquid oxygen vaporized
g_c	force-mass conversion factor, 32.17 (lb mass)(ft)/(lb force)(sec^2); 1(kg)(m)/(N)(sec^2)
H_T^o	sum of sensible enthalpy and chemical energy at temperature T and standard conditions, cal/mole; J/mole
$H_{T,f}^o$	H_T^o of fuel (H_2) at input temperature
H_{T,H_2}^o	H_T^o of fuel (H_2) at local combustion gas temperature
H_{T,H_2O}^o	H_T^o of water vapor (H_2O) at local combustion gas temperature
$H_{T,o}^o$	H_T^o of liquid oxygen (lox) at input temperature

J	4.184×10^7 erg/cal; 4.184 joule/cal
KE	kinetic energy of combustion gas mixture, cal/sec; J/sec
L_c	length of straight combustion chamber, in.; cm
L_n	length of converging nozzle, in.; cm
L_{ef}	effective length for vaporization, in.; cm
$L_{ef,c}$	L_{ef} in cylindrical chamber, in.; cm
$L_{ef,e}$	L_{ef} at nozzle entrance, in.; cm
$L_{ef,n}$	L_{ef} in nozzle, in.; cm
$\mathcal{M}$	molecular weight, kg/mole
N_f	input flow of fuel (H_2), moles/sec
N_o	input flow of liquid oxygen, moles/sec
O/F	oxidant-fuel mass flow ratio
P	pressure lb force/in.^{2}; N/m^2
P_c	measured chamber pressure lb force/in.^{2}; N/m^2
Q	defined by eq. (A7)
R	Gas law constant 1.987 cal/(g-mole)($^\circ$K); 8.314×10^3 J/(kg-mole)($^\circ$K)
S	nozzle shape factor, nozzle volume/(chamber area X L_n)
S^o_T	entropy at temperature T and standard conditions, J/(kg-mole)($^\circ$K)
S^o_{T,H_2}	entropy of fuel (H_2) vapor at local combustion gas temperature
S^o_{T,H_2O}	entropy of water (H_2O) vapor at local combustion gas temperature
T	temperature, $^\circ$K
$T_{l,o,r}$	reduced initial liquid-oxygen temperature, dimensionless
V_a	velocity of air, ft/sec; m/sec
V_j	velocity of liquid jet, ft/sec; m/sec
V_o	initial liquid-oxygen velocity, ft/sec; m/sec
W	mass flow rate, lb mass/sec; kg/sec
W_a	mass flow rate of air, lb mass/sec; kg/sec
W_f	mass flow rate of fuel (H_2) at injector, lb mass/sec; kg/sec
W_j	mass flow rate of liquid jet, lb mass/sec; kg/sec

W_o mass flow rate of oxygen at injector, lb mass/sec; kg/sec

X_c length from injector in chamber, in.; cm

X_n lenght from nozzle entrance in nozzle, in.; cm

α exponent (see eq. (A12))

β defined by eq. (A11)

η_{C*} characteristic exhaust velocity efficiency, percent of theoretical

γ specific heat ratio

ρ_j density of liquid, lb mass/ft^3; kg/m^3

Subscripts:

g total combustion gas mixture

t nozzle throat

1, 2, . . . refers to position as in fig. 14

APPARATUS AND PROCEDURE

Rocket Combustors

The combustor dimensions, nominal chamber pressure levels, and corresponding propellant flow rates are given in table I. The injector, chamber, and nozzles were separate detachable units. The combustor is illustrated in figure 1. The chambers were solid copper, but the nozzles were provided with internal passages for water cooling. The entire engine was cooled by an external water spray.

Single-element concentric-tube injectors (see fig. 2) were used with liquid oxygen injected from the central tube surrounded by an annular flow of gaseous hydrogen. During the program, the central tube was easily bent off-axis, and the tube tip had a tendency to erode. This problem was eliminated by providing the injectors with braces (shown in fig. 2) to position the tube and conduct heat away from the tube to the injector face. The inner diameter of the central tube was 0.116 inch (0.295 cm). The inner and outer diameters of the annulus were 0.156 (0.396 cm) and 0.325 inch (0.825 cm), respectively. The braces were approximately 0.06 inch wide (0.153 cm) and occupied about 24 percent of the annular flow area. The dimensions of all the injectors used for the program were identical. Some, however, were constructed of stainless steel and others of copper.

Flat unserrated surfaces were used between the various combustor surfaces. Sealing was accomplished by means of silicone rubber gasket rings inserted in flat-faced grooves between the sections, as shown in figure 1.

Instrumentation

Chamber pressure was measured with a strain-gage tranducer connected to the chamber 1 inch (0.0254 m) downstream of the injector face. The upper frequency response of the chamber pressure measurement system was approximately 200 cycles per second (200 Hz).

Gaseous-hydrogen flow rates were measured with a sharp-edged subsonic orifice, from which mass flow was calculated from measurements of upstream pressure, temperature, and pressure drop across the orifice. Liquid-oxygen mass flow rate was measured with a turbine-type flowmeter. The output signal of the alternating-current flowmeter was converted to a direct-current signal proportional to the flow rate.

All measurements were made from strip-chart pen recorders. The accuracy in the characteristic exhaust velocity C* when determined with this type of system is approximately ±1 percent.

Operation Procedure

Each run consisted of three stages: ignition, low flow, and full flow operation. Ignition was established by the hypergolic action of gaseous hydrogen with gaseous fluorine. After ignition, liquid oxygen at a reduced flow was allowed to enter the combustor. The gaseous-fluorine flow was then stopped, and a low pressure hydrogen-oxygen (H_2-O_2) flame was established. The fire valves were then fully opened to permit operation at full propellant flow. Steady-state operation during which data were taken was maintained for approximately $1\frac{1}{2}$ to $2\frac{1}{2}$ seconds, the longer time being required at the lower pressures.

Propellant feed was accomplished by means of a pressurized tank system. The oxygen tank and feed system were submerged in boiling liquid nitrogen exposed to atmospheric pressure. The injection temperature of the liquid oxygen was therefore at approximately the boiling temperature of liquid nitrogen (78° K). The gaseous hydrogen was injected at ambient temperature (approx. $60\pm20^{\circ}$ F or $290\pm11^{\circ}$ K).

RESULTS AND DISCUSSION

General Observations

No combustor erosion or burnout problems were encountered at chamber pressures below approximately 1600 psia (1.10×10^7 N/m^2 absolute). At higher pressures, chamber

and nozzle erosion did occur. Damage was always greater in the combustor with a low contraction ratio. This difference was probably due to the fact that the chamber gas velocity varies inversely with contraction ratio. Erosion, when it did occur, took place in the chamber near the nozzle inlet end and in the nozzle section. The nozzle of the combustor with a low contraction ratio was severely eroded after only two runs at approximately 2000 psi (1.38×10^7 N/m^2 absolute) with a 2-inch-long (5.08-cm-long) chamber. In contrast, the nozzle section with a high contraction ratio at the same chamber pressure survived several tests, each with the 2-inch (5.08-cm) and 4-inch-long (10.16-cm-long) chambers, and was severely eroded after only several runs with the 10-inch-long (25.4-cm-long).

The presence of the braces in the injector seemed to cause much scatter in the performance measurements of the combustor with a high contraction ratio. The braces also seemed to induce a low frequency instability of about 50 to 100 cycles per second (50 to 100 Hz) in the combustor with a high contraction ratio. Therefore, the data obtained with the braced injector for the combustor with a high contraction ratio is not used. The presence of injector braces appeared to have no effect on the operation or performance of the combustor with a low contraction ratio.

Performance Measurements

The experimental results before correction for momentum pressure losses are tabulated in table II and presented graphically in figure 3. The data are grouped so that characteristic exhaust velocity efficiency, a percent of theoretical C*, is a function of measured chamber pressure with chamber length as a parameter. The efficiencies in table II were based on a theoretical C* calculated for gaseous hydrogen and liquid oxygen with the use of the method of reference 6. Most of the data points represent an arithmetic mean of five or more successive runs. A few points, however, represent single runs and are so indicated in figure 3 and in table II.

The experimental data indicate an increase of performance efficiencies with increasing chamber pressure for the combustors with a low contraction ratio. It is observed that some of the efficiencies exceed 100 percent. The measurements are not thought to be a function of the instrumentation system, as various transducers were used to recheck the measurements, and the system was frequently calibrated. In contrast to the low-contraction-ratio data, the high-contraction-ratio data exhibited a pronounced performance loss with increasing pressure for the 2- and 4-inch-long (5.08- and 10.16 cm long) chambers.

Momentum pressure loss. - To explain the performance above 100 percent, a momentum pressure loss might be applied as in reference 7. If all the combustion is as-

sumed to occur before the nozzle entrance, a correction of +5 percent can be applied for a contraction ratio of 2, while virtually no correction can be applied for a contraction ratio of 10. This momentum pressure loss correction would still indicate performances above 100 percent. If, however, the extreme case of combustion near sonic velocity is considered, a correction of 25 percent could be applied (ref. 7). Thus for complete combustion, the apparent C* efficiency could be between 105 and 125 percent. It might be suspected, therefore, that the actual combustion is occurring somewhere between these two extremes.

In view of the foregoing, the combustion model discussed more completely in appendix A was developed. The continuity, momentum, and energy equations are simultaneously satisified at every location in the combustion chamber and nozzles. The results of the vaporization model of Priem and Heidmann (ref. 4) were used to determine the percent of liquid oxygen vaporized at every location in the combustion chamber and nozzle. Combustion in the nozzle was thus allowed, and if sufficient burning at a high Mach number can be obtained, large losses in total pressure will result.

Effect of atomization model on C* efficiency. - The vaporization model (ref. 4) requires the knowledge of the mass median drop radius to calculate the percent of liquid oxygen vaporized. If it is assumed, as in reference 4, that the drop size is a function only of the liquid-oxygen jet diameter, the drop size for all the runs reported herein would be constant. Figure 4 shows the results of the combustion model under this assumption of a constant initial drop size of 300 microns, which gives the best fit of the data at low pressures. The C* efficiencies η_{C^*} were determined with the use of the calculated pressure at the experimental transducer location (1 in. from the injector (2.54 cm)). It can be seen that η_{C^*} increased with pressure for all chamber lengths and contraction ratios with an assumed constant drop size. Although good agreement is obtained for the 2-inch chamber with a contraction ratio of 2, the obtained η_{C^*} fails to agree with even the trends of the other data. A constant initial drop size does not appear to be a good assumption for these data.

The drop size correlation presented in appendix B predicts that the mass median drop diameter would increase in proportion to the square root of the chamber pressure at a constant oxidant-fuel ratio and injector geometry. For liquid oxygen at 78° K, gaseous hydrogen at 298° K, an oxidant-fuel ratio of 2.3, and a chamber geometry as shown in figure 2, the relation is $D_m = 15.45\sqrt{P_c}$, where D_m is in microns and P_c is in psia. Figure 5 shows the results of the combustion model with the drop size correlation assumption. It is apparent that good agreement is obtained for the performance trends of the combustor with a large contraction ratio for chamber lenghts of 2 and 4 inches (4.08 and 10.16 cm). The increasing drop size may very well be the reason for the decreasing performance with increasing chamber pressure. The performance trends for the rest of the data are, however, not accurately predicted.

From the preceding it would at first appear that different atomization mechanisms were occurring that depend on the contraction ratio and chamber length. The combustion gas velocity for the contraction ratio of 2 is higher than that for a ratio of 10, but the cold hydrogen velocity from the injector should be dominant in both cases in the region near the injector where atomization occurs. A change in jet atomization with increasing chamber length also does not seem likely. Some other phenomena appears to be dominant at high pressures and large chamber lengths.

Flash vaporization model. - For a large chamber length, a low contraction ratio, and a pressure near or exceeding the critical pressure of oxygen, the liquid-oxygen drops remaining at the nozzle entrance may attain a temperature approaching the critical temperature. Reference 8 indicates that for a uniform liquid-oxygen spray the droplets may approach their critical temperature in the length necessary to vaporize only 5 percent of the drop mass. Upon entering the nozzle, these drops will experience a rapidly dropping pressure that could cause a very rapid or flash vaporization of the drops. This oxygen vapor then only need be properly mixed with the surrounding hydrogen gas to complete the combustion. These phenomena would result in increased burning near sonic velocity, which would increase the total pressure loss necessary for apparent efficiencies above 100 percent.

To accommodate the aforementioned phenomena, the vaporization model (ref. 4) was altered by multiplying that portion of the effective length (see appendix A) which governs vaporization in the nozzle by $e^{\alpha X_n^2}$ where X_n is the distance from the nozzle entrance. The value of α for each operating condition can be calculated from equations (A11) and (A12) of appendix A. These equations are an empirical correlation for α of the data reported herein.

Results of flash vaporization model. - Figure 6 shows the results of the final combustion model, including the drop size correlation of appendix B and the flash vaporization in the nozzle. The prediction of performance trends is excellent for all conditions. An apparent C* efficiency, based on the static pressure at the transducer, of as high as 107.5 percent is obtained. The reason for these high apparent C* efficiencies can be seen from an examination of figure 7 in which the total pressure at the nozzle throat is related to the total pressure at the injector. The total pressure loss from the injector to the throat should be reflected in η_{C^*} and thus the throat total pressure should be used in the calculation of C*. This results in η_{C^*} curves whose values do not exceed 100 percent, as shown in figure 8. In figure 7 it is shown that the total pressure loss (especially for short chambers and high pressures) greatly exceeds that predicted from reference 7 (negligible for $\mathscr{A} = 10$, and 5 percent for $\mathscr{A} = 2$). For low pressures and large chamber lengths, the total pressure loss approaches that of reference 7. This condition can be expected since the smaller drop size and large chamber length result

in a large percentage of the combustion occurring before the nozzle entrance and very little combustion occurring in the nozzle.

The sensitivity of the calculated apparent C* efficiency to the oxidant-fuel ratio is shown in figure 9. The O/F effect is great, especially at high chamber pressures. Much of the experimental scatter may be due to the inability to hold a constant oxidant-fuel ratio of 2.3.

The need for the flash vaporization model or an alternate can be seen from figure 10. The combustion model without flash vaporization was used to calculate the drop size D_{mi} necessary to attain the measured chamber pressure. When D_{mi} was compared with the correlated drop size D_{mc} (appendix B) and plotted against the effective length at the nozzle entrance, several interesting points were noted. For pressures below the oxygen critical pressure, $D_{mi} \approx D_{mc}$ no matter what the value of the effective length. For short effective lengths (assymptotic to $L_{ef} \approx 0.5$), $D_{mi} \approx D_{mc}$ even for chamber pressures above the critical pressure. However, for large effective lengths and with chamber pressures above critical, $D_{mi} \neq D_{mc}$. These results would indicate that for conditions in which the liquid-oxygen drops could not approach the critical temperature the vaporization model (ref. 4), along with the drop size correlation of appendix B, provides a good representation of the experimental results. However, when a sufficient amount of the liquid-oxygen drops approach the critical temperature, the model of reference 4 is not valid. It is quite apparent that for supercritical pressures and an L_{ef} at the nozzle entrance much above 0.5, an alternate to the vaporization model of reference 4 must be used.

The data points of figure 10 that are marked with an arrow represent runs in which the measured chamber pressure could not be attained in the calculations no matter how small the drop size was assumed. The calculations were thus terminated when the effective length for vaporization at the nozzle throat exceeded 20.

CONCLUDING REMARKS

Performance efficiency, in terms of characteristic exhaust velocity, was measured for gaseous-hydrogen - liquid-oxygen rocket combustors over an extended range of chamber pressures, from approximately 300 to 1800 psia (2.06×10^6 to 1.24×10^7 N/m^2 absolute). The pressure range was covered with two series of combustors, one had a low contraction ratio of 2 and the other had a high contraction ratio of 10. The oxidant-fuel mixture ratio was held constant at approximately 2.3 (±10 percent) which corresponds to maximum theoretical characteristic exhaust velocity.

The following results were obtained:

1. The apparent efficiency of the characteristics exhaust velocity (calculated by using the measured chamber pressure at the injector end) of combustors with a contraction ratio of 2 increased with increasing chamber pressure over the entire pressure range.

2. The apparent characteristic exhaust velocity efficiency of combustors with a contraction ratio of 10 showed a decrease with increasing pressure for chamber lengths of 2 and 4 inches (5.08 and 10.16 cm). Performance efficiency of a 10-inch-long (25.4-cm-long) chamber increased very slightly with pressure.

3. Calculated performance increased with increasing pressure for all combustors for this program, with an assumed constant initial drop size and vaporization-controlled combustion. These calculations were successful in predicting performance trends for the low but not for the high contraction ratio combustors.

4. Calculations based on the vaporization model with drop size increasing proportional to the square root of chamber pressure predicted a performance decrease with increasing chamber pressure. These calculations successfully predicted performance trends for subcritical chamber pressures and for supercritical chamber pressures when the effective length for vaporization was low at the nozzle entrance.

5. When the vaporization model of item 4 was modified to include flash vaporization and combustion in the nozzle, the performance trends for all the data were successfully predicted.

6. It has been suggested previously that at high pressures a large fraction of liquid oxygen in a rocket combustor may attain the critical point. The results of this program indicate that this situation may occur when the effective length for vaporization at the nozzle entrance exceeds 0.5 inch (1.27 cm). Flash vaporization may then occur in the nozzle.

7. Large losses of total pressure can occur due to combustion in the nozzle. A total pressure loss, between the injector and the nozzle throat, of as much as 12 percent was calculated with combustion in the nozzle, while a more conventional technique assuming isentropic expansion in the nozzle predicted only a 5-percent loss. The apparent characteristic exhaust velocity efficiency, based on the measured chamber pressure near the injector, can thus significantly exceed 100 percent.

8. Combustion of liquid oxygen beyond its critical pressure can result in increased characteristic exhaust velocity efficiency due to flash vaporization and combustion in the nozzle, but this efficiency is attained at the expense of the accompanying total pressure loss.

Lewis Research Center,
National Aeronautics and Space Administration,
Cleveland, Ohio, May 23, 1967,
128-31-06-03-22.

APPENDIX A

BURNING IN NOZZLE AND COMBUSTION ABOVE CRITICAL PRESSURE

Combustion Model

The following combustion model was developed to satisfy the energy, momentum, and continuity equations at each position in the combustor. It is assumed that the ideal gas equation of state may be applied and that the number of moles of combustion products remains constant, which follows from the assumption of the simple H_2-O_2 reaction in which each mole of hydrogen consumed produces a mole of water. This assumption is true if combustion is complete and if the products contain no dissociation species, and it is valid at low oxidant-fuel mixture ratios and for completely mixed gases.

The momentum and kinetic energy of the liquid oxygen were not considered in the following equations. At the injector, where the approximation is least accurate, the momentum ratio of gas to liquid was between 4 and 20 for the data considered, and this ratio will increase away from the injector. Neglecting the liquid-oxygen kinetic energy was even less consequential than neglecting the momentum due to the high ratio of gas to liquid velocity. Only gaseous products were considered in continuity due to the small fraction of the volume occupied by the liquid.

The energy equation as used was

$$2N_O F H^O_{T,\,H_2O} + (N_f - 2N_O F) H^O_{T,\,H_2} + N_O(1 - F) H^O_{T,\,O} + KE = N_f H^O_{T,\,f} + N_O H^O_{T,\,O} \tag{A1}$$

The momentum equation for flow between two locations of a straight section of the combustor was

$$P_1 - P_2 = \frac{JRN_f}{g_c A^2}\left(\frac{W_2 T_2}{P_2} - \frac{W_1 T_1}{P_1}\right) \tag{A2}$$

The kinetic energy can be expressed as

$$KE = \frac{JR^2 N_f^2 W_g T^2}{2 g_c A^2 P^2} \tag{A3}$$

and for the case of sonic velocity at the throat,

$$KE_t = \frac{RN_f \gamma_t T_t}{2} \tag{A4}$$

When the fraction of the liquid oxygen vaporized F is prescribed at each location in the straight section of the combustor and a pressure given at some location, the temperature and pressure can be calculated from equations (A1) and (A2) at every location. The values of H_T^o were obtained from reference 9 and are a function of temperature only.

In the converging section of the nozzle, a thermodynamic process must be defined. The process involves simultaneous expansion and burning. The process was approximated by consecutive isentropic expansions and constant area combustion processes, since no single thermodynamic process can describe the actual process. As seen in figure 11, the isentropic expansions from 2 to 3, 4 to 5, etc. were followed by constant area combustion processes from 3 to 4, 5 to 6, etc., respectively. The equation used for the isentropic expansion between points 2 and 3 was

$$2N_o F\left[\left(S_T^o, H_2O\right)_2 - \left(S_T^o, H_2O\right)_3\right] + \left(N_f - 2N_o F\right)\left[\left(S_T^o, H_2\right)_2 - \left(S_T^o, H_2\right)_3\right] = RN_f \log_e\left(\frac{P_2}{P_3}\right) \tag{A5}$$

No combustion occurs during this process and F is calculated at location 2. The values of S_T^o were obtained from reference 9 and are a function of temperature only.

If the combustion process is vaporization limited, the fraction of the liquid oxygen vaporized F can be obtained from reference 4 where the parameter controlling vaporization in the straight combustion chamber is

$$L_{ef,c} = \left(\frac{X_c}{0.44}\right) Q \tag{A6}$$

where

$$Q = \frac{(P_c/300)^{0.66}}{(1 - T_{l,o,r})^{0.4}(D_m/152)^{1.45}(V_o/100)^{0.75}} \tag{A7}$$

and X_c is the distance from the injector (fig. 11). Within the nozzle, the governing parameter is

$$L_{ef,n} = L_{ef,e} + \left(\frac{0.83\, X_n}{\mathscr{A}^{0.22} S^{0.33}} \right) Q \tag{A8}$$

Where $L_{ef,e}$ is the effective length at the nozzle entrance and is $L_{ef,c}$ evaluated at $X_c = L_c$, and X_n is the distance in the nozzle measured from the nozzle entrance.

When the effective length is determined at any location, F can be determined from figure 12.

When this combustion model was used, the drop sizes necessary to satisfy the experimental pressures were consistently too high for the data for a contraction ratio of 2. This situation is contrary to expectations since the higher combustion gas velocity for a low contraction should, if anything, produce smaller drop sizes. A reexamination of reference 4 revealed that for heptane sprays (the only detailed information given) the curve of F as a function of L_{ef} for high contraction ratios lay near the top of the error band, while that of low contraction ratios lay near the bottom, at least for a large L_{ef}. Consequently, the upper and lower curves of figure 12 were used for contraction ratios of 10 and 2, respectively. These ratios are within, or are very near, the bounds for liquid oxygen given in reference 4.

Combustion Above Critical Pressure

When liquid-oxygen drops entering the nozzle are near the critical temperature (ref. 8), the suddenly decreasing gas pressure can cause a rapid or flash vaporization. The combustion of this oxygen vapor is probably mixing limited, but an attempt was made to account for the phenomena of flash vaporization by an acceleration of the vaporization in the nozzle. Increased combustion in the nozzle was obtained by modifying equation (A8) to yield

$$L_{ef,n} = L_{ef,e} + \frac{0.83\, Q}{\mathscr{A}^{0.22} S^{0.33}} X_n e^{\alpha X_n^2} \tag{A9}$$

Values of α were calculated for each run so that the chamber pressure calculated from the combustion model was equal to the measured chamber pressure. The values of α were fit by the method of least squares to an equation of the form

$$\beta = C_1 \mathscr{A}^{C_2} \left(\frac{P_c}{300}\right)^{C_3} (L_{ef,e} - 0.5) \tag{A10}$$

where C_1, C_2, C_3 are constants. The resulting equation was

$$\beta = 0.08 \mathscr{A}^{-0.52} \left(\frac{P_c}{300}\right)^{2.5} (L_{ef,e} - 0.5) \tag{A11}$$

The correlation was further modified to

$$\alpha = \frac{3.6\beta}{\sqrt{\beta^2 + 9}} \tag{A12}$$

so that exceedingly large values of α were not obtained with large values of β. It can be seen from equation (A12) that for $\beta >> 3$, $\alpha = 3.6$, while for $\beta << 3$, $\alpha = 1.2\ \beta$.

The values of α as well as equation (A12) are plotted in figure 14. Although there is some scatter in the data, equation (A12) predicts the trend of α.

Procedure For Use of Combustion Model

The combustion locations referred to in this section correspond to those shown in figure 11. Although in figure 11 only three isentropic expansion and constant area combustion steps are shown, the calculations made in this report used seven steps. The three steps are shown for illustrative purposes only. More steps should represent a closer approximation to the actual process. The incremental lengths in the nozzle should be chosen smallest near the throat since this is where T and P are changing most rapidly.

An approximate static pressure at position 1 (the injector) is needed first and can be approximated by

$$P_1 = \frac{C^*_{th}(W_o + W_f)}{g_c A_t} \tag{A13}$$

in which an apparent C* efficiency of 100 percent is assumed. The drop size for a concentric tube injector can then be calculated from equation (B3) (appendix B). If some

other injector is used (drop size not dependent on pressure), the drop size may be calculated as in reference 4, and the use of equation (B3) is not necessary.

The effective length for vaporization at each position in the chamber (eq. (A6)) and nozzle (eq. (A8) or (A9)) can be calculated, and the fraction of liquid oxygen vaporized F at each position can be determined from figure 12.

The energy equation (eq. (A1)) when used with equation (A4) at the nozzle throat (position 8) is a function only of throat temperature, which can be determined by iteration. The throat pressure is then determined by

$$P_t = P_8 = \sqrt{\frac{JRT_t W_g N_f}{\gamma_t g_c}} \tag{A14}$$

Equations (A1) and (A2) (eq. (A3) used for KE) will then determine T_7 and P_7, and equations (A1) and (A5) determine P_6 and T_6. This iteration is repeated for each isentropic expansion and constant area burning step until the nozzle entrance conditions are determined (position 2).

The temperature and pressure at any location in the straight chamber (such as position 1) can then be determined by the use of equations (A1) and (A2). If the combustion chamber is tapered, the procedure used for the nozzle must be continued for the combustion chamber.

If the drop size is not dependent on chamber pressure (drop size determined from ref. 4), the calculation is completed and temperature and pressure are determined at each location in the engine. For a concentric tube injector, however, the new P_1 must be used to correct the drop size and the foregoing calculation procedure repeated. The third repetition of the calculation loop will usually suffice, since after this P_1 will change insignificantly.

Because of the obvious length of these calculations, they were performed on the Lewis Research Center IBM 7090 computer.

APPENDIX B

CORRELATION OF CONCENTRIC-TUBE DROP SIZE

A study of the drop size obtained from a concentric-tube injector similar to that of figure 2 was made. Water was injected from the center tube and air from the annulus. Photographs of the resulting spray were analyzed to determine the drop size distribution from which the mass median drop diameter was determined.

The variables investigated were the gas annular area (5.65×10^{-3} to 6.36×10^{-2} in.^{2}; 0.0364 to 0.410 cm^2; 5 areas), liquid jet diameter (0.06 and 0.09 in.; 0.152 and 0.229 cm) and velocity (25 and 50 ft/sec or 7.62 and 15.2 m/sec), and relative velocity between the gas and the liquid jet (300 to 1000 ft/sec or 91.2 to 304 m/sec; 4 values). The injector discharged into ambient air.

The ratio of the mass median drop diameter D_m to the liquid jet diameter D_j is plotted against the square root of the ratio of the gas to liquid momentum (fig. 14). It can be seen that for high momenum ratios the following correlation is valid:

$$\frac{D_m}{D_j} = 1.5\sqrt{\frac{W_j V_j}{W_a V_a}} \tag{B1}$$

Using the ideal gas equation of state and the continuity equation yields

$$D_m = 1.5\,\frac{W_j}{W_a}\sqrt{\frac{4\mathcal{M}_a A_a P_a}{\pi R \rho_j T_a}} \tag{B2}$$

To use equation (B2) for the combustion data of this report, hydrogen properties were substituted for air properties and liquid-oxygen properties for water properties, chamber pressure was used, and equation (B2) was multiplied by 0.286. The multiplication was necessary to get the reduced drop size due to the lower surface tension and viscosity of liquid oxygen as compared with water. It should be noted that for a liquid-oxygen - hydrogen injector no significance should be attached to the absolute magnitude of the drop size but only to its trend with pressure. The final drop size correlation used was

$$D_m = 0.485\left(\frac{O}{F}\right)\sqrt{\frac{\mathcal{M}_{H_2} A_{H_2}}{R\rho_j T_{H_2}} P_c} \tag{B3}$$

or with $A_{H_2} = 0.0638$ square inch (0.4116×10^{-4} m^2), $\rho_j = 1.202$ grams per cubic centimeter, $T_{H_2} = 298^{O}$ K, and $O/F = 2.3$

$$D_m = 15.45\sqrt{P_c} \tag{B4}$$

where P_c is in psia and D_m is in microns.

The geometric standard deviation of the water sprays when the drop size distributions were fit to a log-normal distribution was very nearly 2.3.

REFERENCES

1. Hersch, Martin: Combined Effects of Contraction Ratio and Chamber Pressure on the Performance of a Gaseous Hydrogen-Liquid-Oxygen Combustor for a Given Propellant Weight Flow and Oxidant-Fuel Ratio. NASA TN D-129, 1961.

2. Hersch, Martin: Effect of Interchanging Propellants on Rocket Combustor Performance with Coaxial Injection. NASA TN D-2169, 1964.

3. Clark, Bruce J.; Hersch, Martin; and Priem, Richard J.: Propellant Vaporization as a Criterion for Rocket-Engine Design; Experimental Performance, Vaporization, and Heat-Transfer Rates with Various Propellant Combinations. NASA Memo 12-29-58 E, 1959.

4. Priem, Richard J.; and Heidmann, Marcus F.: Propellant Vaporization as a Design Criterion for Rocket-Engine Combustion Chambers. NASA TR R-67, 1960.

5. Beichel, R.: High Chamber Pressure Operation for Launch Vehicle Engines Program. Rep. No. 4008-SA4-F (NASA CR-56672), Aerojet-General Corp., June 1, 1964.

6. Gordon, Sanford; and McBride, Bonnie J.: Theoretical Performance of Liquid Hydrogen with Liquid Oxygen as a Rocket Propellant. NASA Memo 5-21-59 E, 1959.

7. Sutton, George P.: Rocket Propulsion Elements. Second ed., John Wiley and Sons, Inc., 1956.

8. Wieber, Paul R.: Calculated Temperature Histories of Vaporizing Droplets to the Critical Point. AIAA J., vol. 1, no. 12, Dec. 1963, pp. 2764-2770.

9. Huff, Veare N.; Gordon, Sanford; and Morrell, Virginia E.: General Method and Thermodynamic Tables for Computation of Equilibrium Composition and Temperatures of Chemical Reactions. NACA TR 1037, 1951.

TABLE I. - NOMINAL COMBUSTOR DIMENSIONS AND OPERATING CONDITIONS

Chamber pressure for 100 percent C*, P_c		Nozzle throat diameter, D_t		Chamber diameter D_c for contraction ratio, $\mathscr{A}$				Flow rate, W				Thrust for 100 percent C*	
				$\mathscr{A}$ = 2		$\mathscr{A}$ = 10		lb mass/sec	kg/sec	lb mass/sec	kg/sec		
								Liquid oxygen		Hydrogen			
psia	N/m^2	in.	cm	in.	cm	in.	cm					lb force	N
400	2.76×10^6	0.530	1.35	0.750	1.91	1.68	4.267	0.240	0.109	0.104	0.0472	89	396
800	5.52×10^6	.445	1.13	.630	1.60	1.41	3.581	.340	.154	.148	.0672	125	556
1200	8.27×10^6	.403	1.02	.568	1.44	1.28	3.251	.415	.188	.180	.0816	155	689
1600	1.10×10^7	.374	.950	.530	1.35	1.18	2.997	.480	.218	.208	.0943	178	702
2000	1.38×10^7	.356	.904	.504	1.28	1.13	2.870	.536	.243	.233	.106	200	890

TABLE II. - EXPERIMENTAL RESULTS OF PERFORMANCE EFFICIENCIES TESTS

Chamber pressure, P_c		Performance efficiency, η_{C^*}, percent	Oxygen flow rate, W_o		Fuel flow rate, W_f		Oxidant-fuel ratio, O/F	Chamber diameter, D_c		Nozzle throat diameter, D_t	
psia	N/m^2		lb mass/sec	kg/sec	lb mass/sec	kg/sec		in.	cm	in.	cm
Chamber contraction ratio, $\mathscr{A}$, 10; straight combustion chamber length, L_c, 2 inches (5.08 cm)											
327	2.24×10^6	81.6	0.236	0.107	0.103	0.0467	2.291	1.670	4.24	0.528	1.34
334	2.29	79.8	.243	.110	.106	.0481	2.292	1.667	4.23	.524	1.33
655	4.49	76.1	.350	.159	.152	.0690	2.303	1.410	3.58	.438	1.11
667	4.57	79.5	.331	.150	.152	.0690	2.178	1.678	4.26	.435	1.10
873	5.99	71.1	.435	.197	.183	.0830	2.377	1.280	3.25	.407	1.03
986	6.76	77.5	.419	.190	.201	.0912	2.085	1.280	3.25	.400	1.02
1097	7.52	67.6	.477	.217	.213	.0967	2.239	1.179	2.99	.374	0.950
1100	7.55	74.0	.438	.199	.213	.0967	2.056	1.279	3.25	.379	.963
1140	7.82	71.2	.471	.214	.195	.0885	2.415	1.177	2.99	.370	.940
Chamber contraction ratio, $\mathscr{A}$, 10; straight combustion length, L_c, 4 inches (10.16 cm)											
347	2.38×10^6	87.4	0.229	0.104	0.102	0.0463	2.245	1.671	4.24	0.524	1.33
715	4.90	86.5	.333	.151	.154	.0694	2.162	1.408	3.57	.440	1.12
998	6.85	82.6	.428	.194	.177	.0803	2.418	1.280	3.25	.406	1.03
1017	6.98	85.5	.399	.181	.183	.0830	2.180	1.279	3.25	.401	1.02
1302	8.93	78.5	.484	.219	.214	.0971	2.262	1.184	3.00	.372	0.945
Chamber contraction ratio, $\mathscr{A}$, 10; straight combustion chamber length, L_c, 10 inches (25.4 cm)											
396	2.72×10^6	97.6	0.240	0.109	0.102	0.0463	2.353	1.681	4.267	0.527	1.34
825	5.66	98.3	.344	.156	.150	.0681	2.293	1.413	3.59	.440	1.12
1190	8.16	102.2	.400	.182	.169	.0767	2.367	1.281	3.25	.401	1.02
1200	8.23	101.7	.409	.186	.183	.0831	2.235	1.280	3.25	.406	1.03
1549	10.62	96.9	.472	.214	.193	.0876	2.446	1.183	3.00	.370	0.940

TABLE II. - Concluded. EXPERIMENTAL RESULTS OF PERFORMANCE EFFICIENCIES TESTS

Chamber pressure, P_c,		Performance efficiency, η_{C^*}, percent	Oxygen flow rate, W_o		Fuel flow rate, W_f		Oxidant-fuel ratio, O/F	Chamber diameter, D_c		Nozzle throat diameter, D_t	
psia	N/m^2		lb mass/sec	kg/sec	lb mass/sec	kg/sec		in.	cm	in.	cm
Chamber contraction ratio, $\mathscr{A}$, 2; straight combustion chamber length, L_c, 2 inches (5.08 cm)											
323	2.22×10^6	78.5	0.242	0.110	0.106	0.0481	2.283	0.748	1.90	0.528	1.34
[a]349	[a]2.39	[a]83.4	[a].247	[a].112	[a].107	[a].0485	[a]2.308	[a].750	[a]1.91	[a].528	[a]1.34
[a]351	[a]2.34	[a]86.2	[a].239	[a].109	[a].107	[a].0485	[a]2.234	[a].751	[a]1.91	[a].529	[a]1.34
[a]767	[a]5.26	[a]86.7	[a].339	[a].154	[a].144	[a].0653	[a]2.354	[a].634	[a]1.61	[a].424	[a]1.08
1081	7.42	88.7	.408	.185	.182	.0826	2.242	.571	1.45	.399	1.01
1127	7.73	91.6	.394	.179	.208	.0944	1.894	.571	1.45	.400	1.02
[a]1192	[a]8.17	[a]90.7	[a].417	[a].189	[a].188	[a].0854	[a]2.218	[a].571	[a]1.45	[a].389	[a]0.988
1537	10.54	90.0	.497	.225	.210	.0953	2.367	.529	1.34	.369	.937
[a, b]1845	[a, b]12.66	[a, b]97.9	[a, b].530	[a, b].240	[a, b].195	[a, b].0885	[a, b]2.718	[a, b].504	[a, b]1.28	[a, b].356	[a, b].904
Chamber contraction ratio, $\mathscr{A}$, 2; straight combustion chamber length, L_c, 6 inches (15.24 cm)											
[a]388	2.66×10^6	[a]98.4	[a]0.231	[a]0.105	[a]0.103	[a]0.0467	[a]2.243	[a]0.754	[a]1.92	[a]0.528	[a]1.34
[a]882	6.05	[a]103.1	[a].327	[a].149	[a].143	[a].0649	[a]2.287	[a].630	[a]1.60	[a].425	[a]1.08
918	6.29	106.4	.350	.159	.132	.0599	2.652	.622	1.58	.429	1.09
1245	8.54	107.6	.392	.178	.168	.0762	2.333	.567	1.44	.399	1.09
1273	8.73	108.9	.394	.179	.172	.0780	2.291	.567	1.44	.399	1.09
[b]1610	[b]11.04	[b]107.6	[b].423	[b].192	[b].198	[b].0989	[b]2.136	[b].529	[b]1.34	[b].369	[b]0.937
[a]1660	[a]11.38	[a]117.0	[a].419	[a].190	[a].188	[a].0853	[a]2.229	[a].530	[a]1.34	[a].375	[a].952
Chamber contraction ratio, $\mathscr{A}$, 2; straight combustion chamber length, L_c, 10 inches (25.4 cm)											
[a]407	$[a]2.79\times10^6$	[a]99.1	[a]0.246	[a]0.112	[a]0.103	[a]0.0468	[a]2.388	[a]0.751	[a]1.91	[a]0.529	[a]1.34
848	5.82	108.1	.308	.140	.144	.0653	2.139	.624	1.58	.435	1.10
881	6.04	110.2	.317	.144	.148	.0672	2.142	.630	1.60	.437	1.11
888	6.09	104.1	.336	.153	.141	.0640	2.383	.618	1.57	.429	1.09
[a]900	[a]6.17	[a]103.1	[a].332	[a].151	[a].145	[a].0658	[a]2.290	[a].630	[a]1.60	[a].424	[a]1.08
922	6.32	109.0	.338	.153	.135	.0613	2.504	.620	1.57	.429	1.09
1287	8.83	105.1	.393	.178	.177	.0804	2.220	.568	1.44	.391	0.993
[a]1500	[a]10.29	[a]100.2	[a].488	[a].221	.235	[a].1067	[a]2.077	[a].530	[a]1.34	.398	[a]1.01

[a]Braced injectors.

[b]Single run.

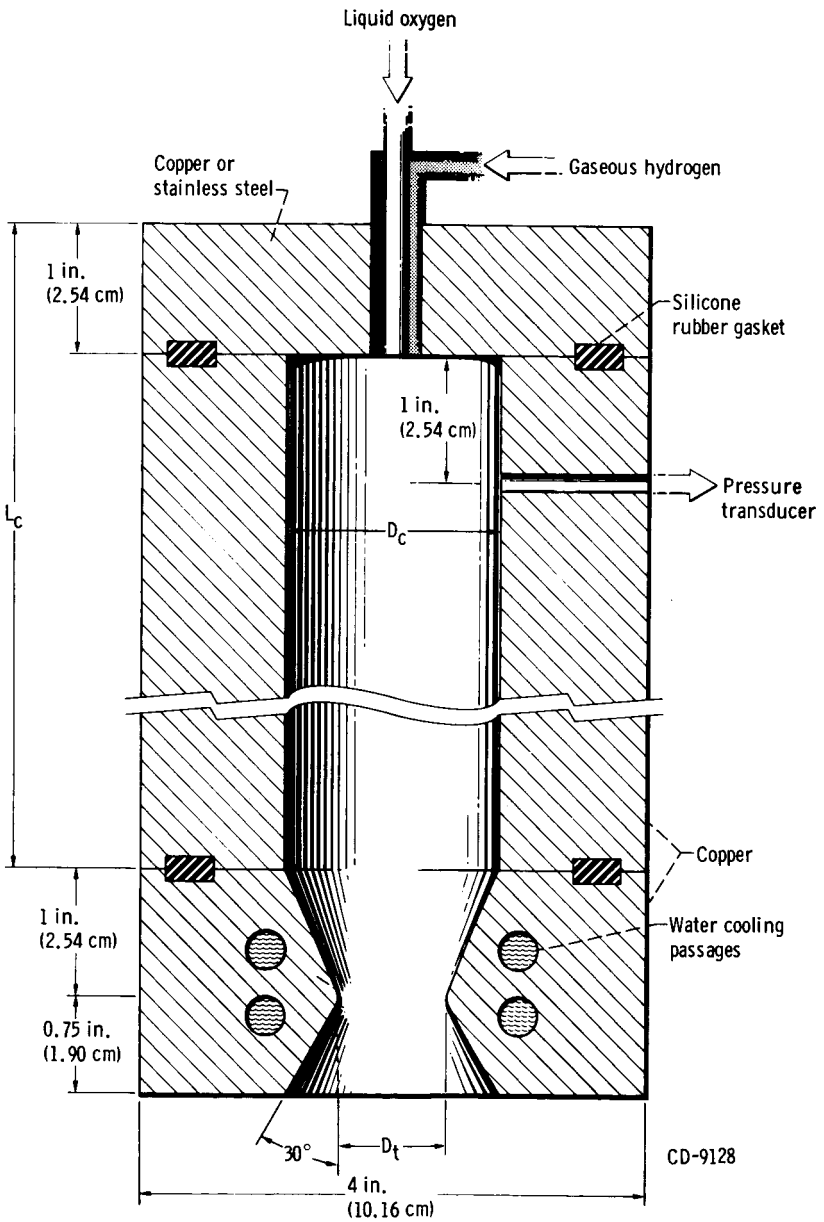

Figure 1. - Combustor.

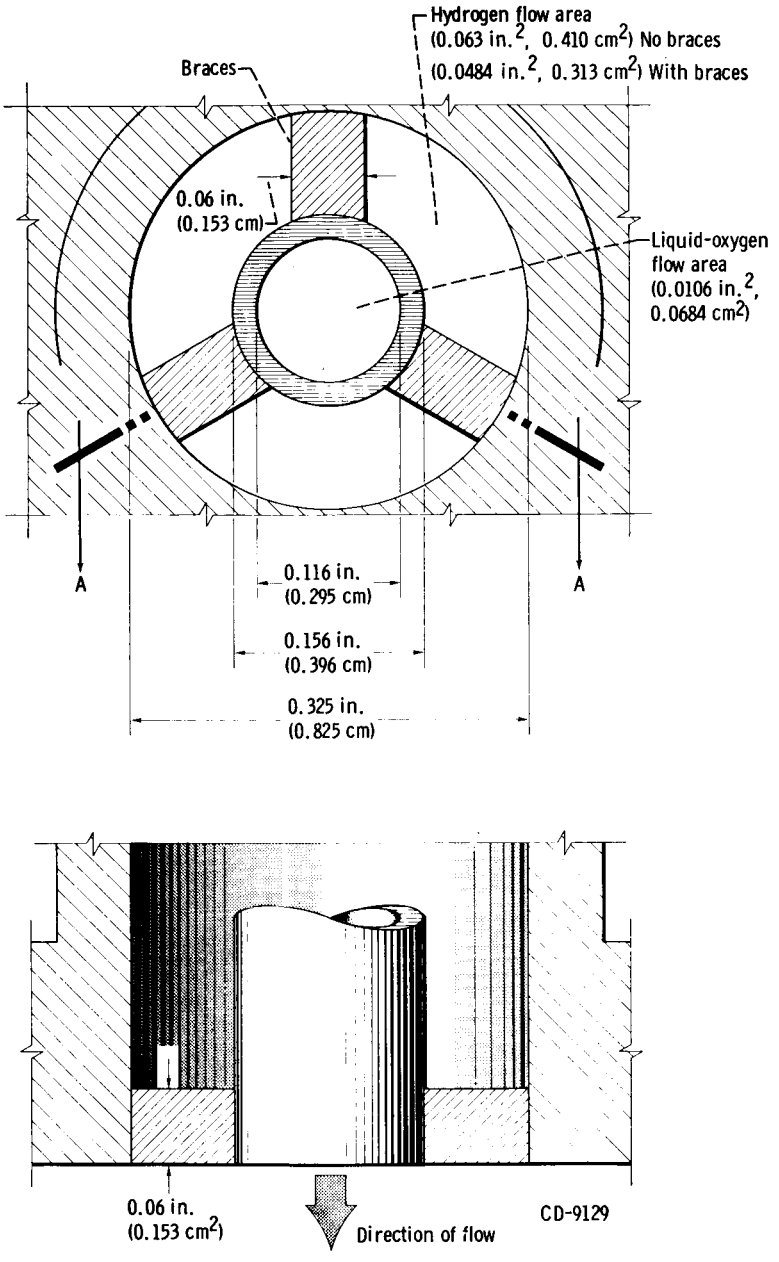

Section A-A

Figure 2. - Injector element.

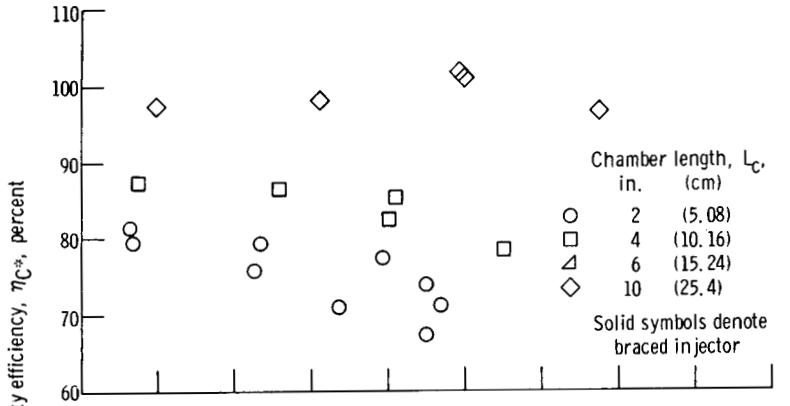

(a) Chamber contraction ratio, 10.

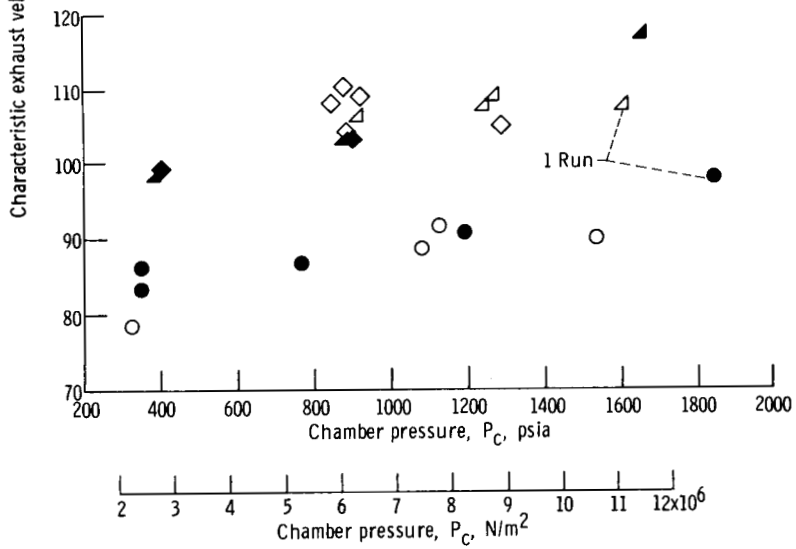

(b) Chamber contraction ratio, 2.

Figure 3. - Experimental characteristic exhaust velocity efficiency against measured chamber pressure.

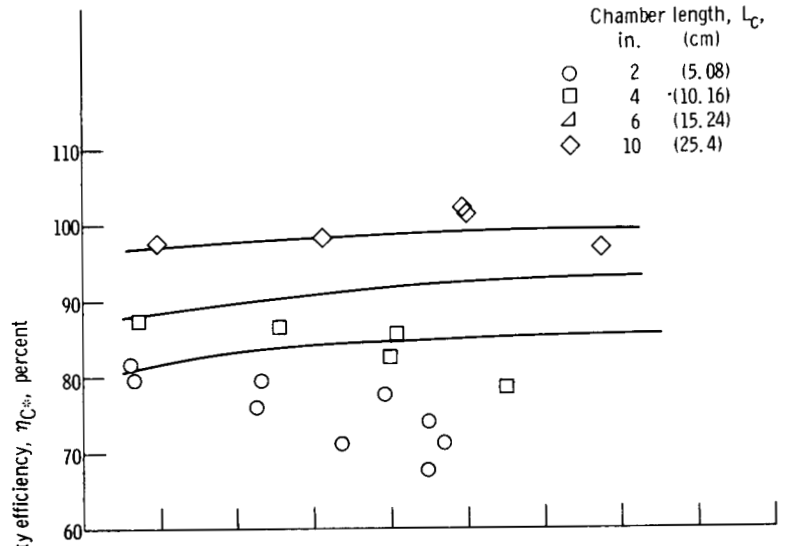

(a) Chamber contraction ratio, 10.

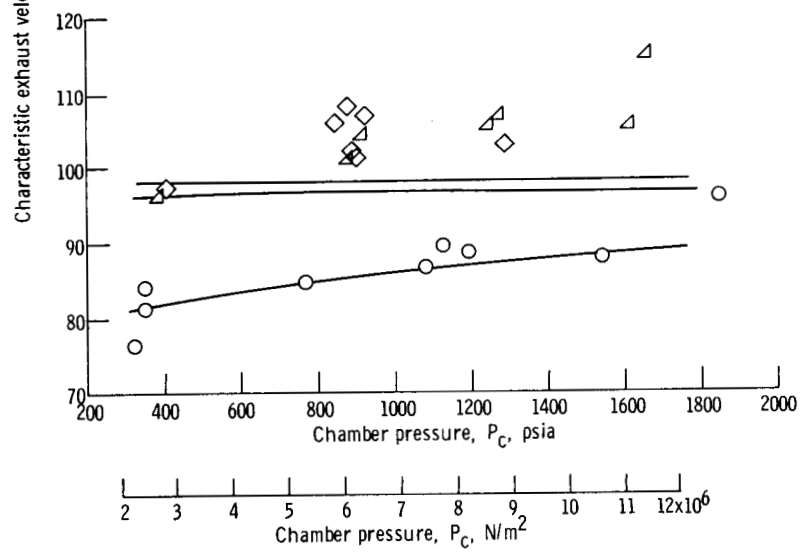

(b) Chamber contraction ratio, 2.

Figure 4. - Comparison of experimental characteristic exhaust velocity efficiency with calculated characteristic exhaust velocity efficiency. Constant initial drop diameter, 300 microns.

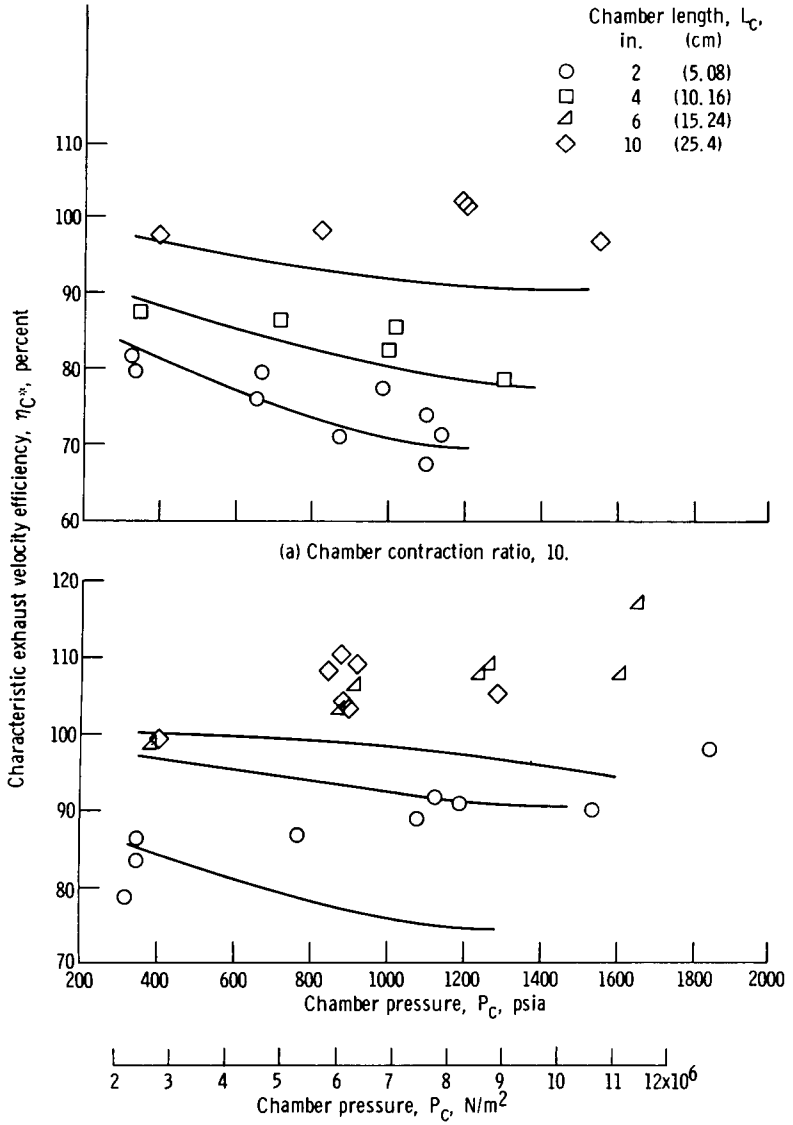

(a) Chamber contraction ratio, 10.

(b) Chamber contraction ratio, 2.

Figure 5. - Comparison of experimental characteristic exhaust velocity efficiency with calculated characteristic exhaust velocity efficiency. Drop size correlation of appendix B used.

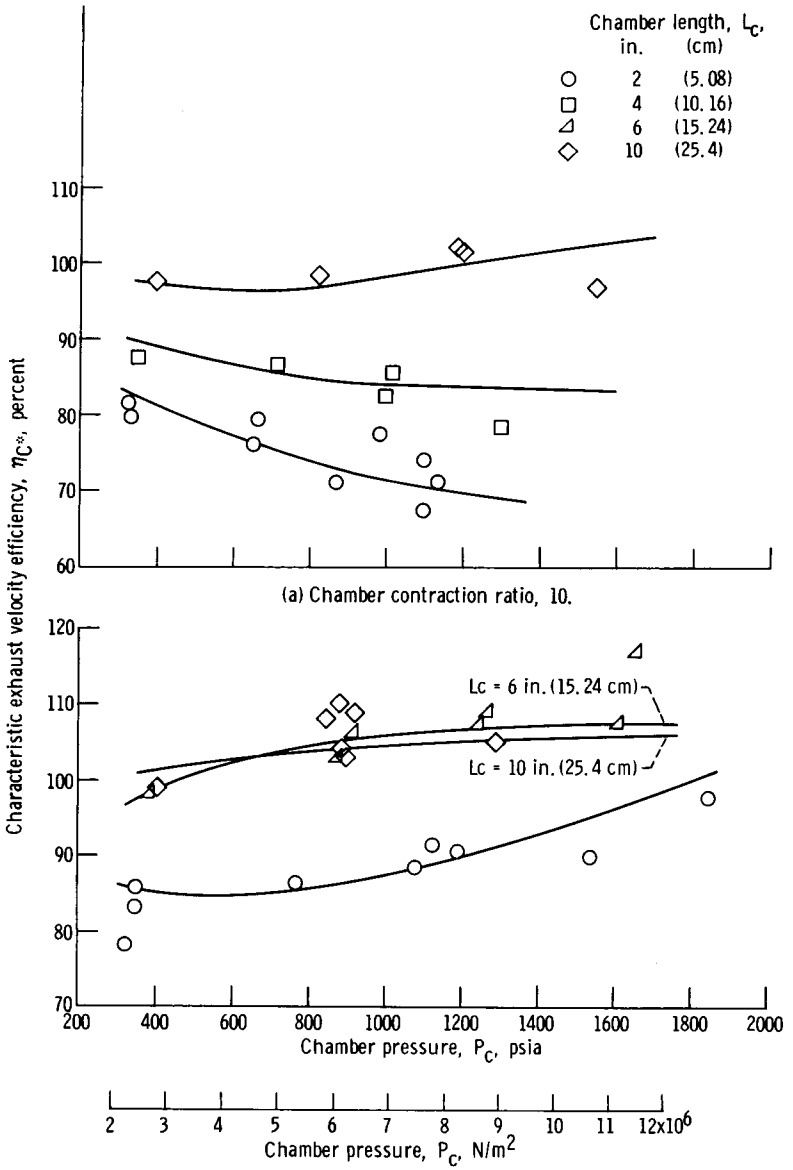

(a) Chamber contraction ratio, 10.

(b) Chamber contraction ratio, 2.

Figure 6. - Comparison of experimental characteristic exhaust velocity efficiency with calculated characteristic exhaust velocity efficiency. Drop size correlation of appendix B and flash vaporization in nozzle used.

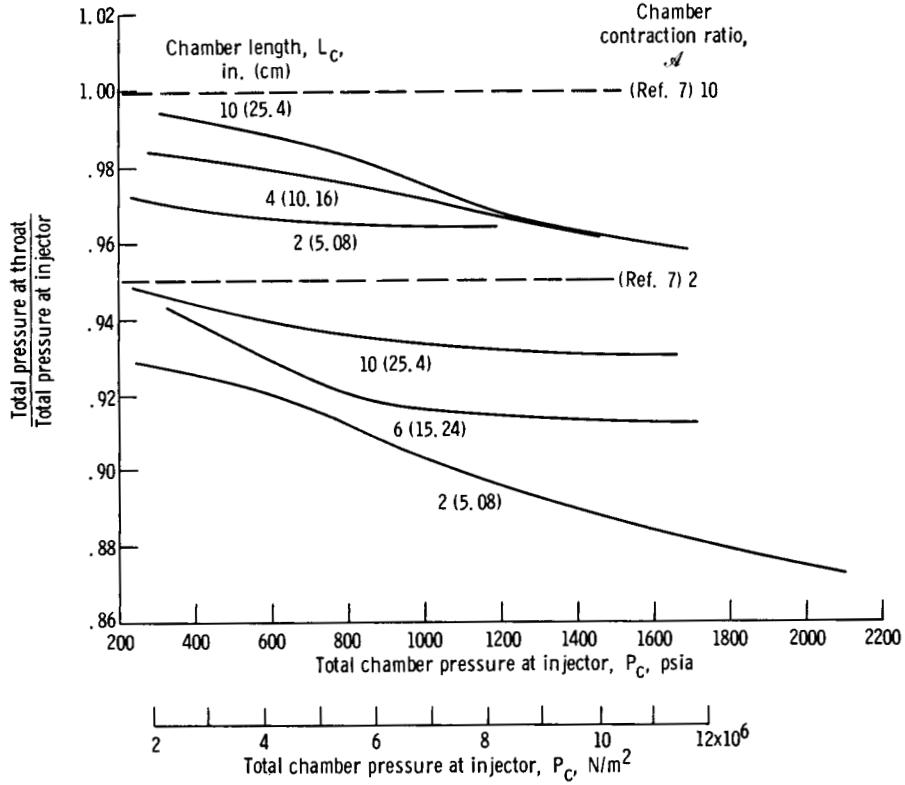

Figure 7. - Total pressure loss with complete combustion model. Oxidant-fuel ratio, 2.3.

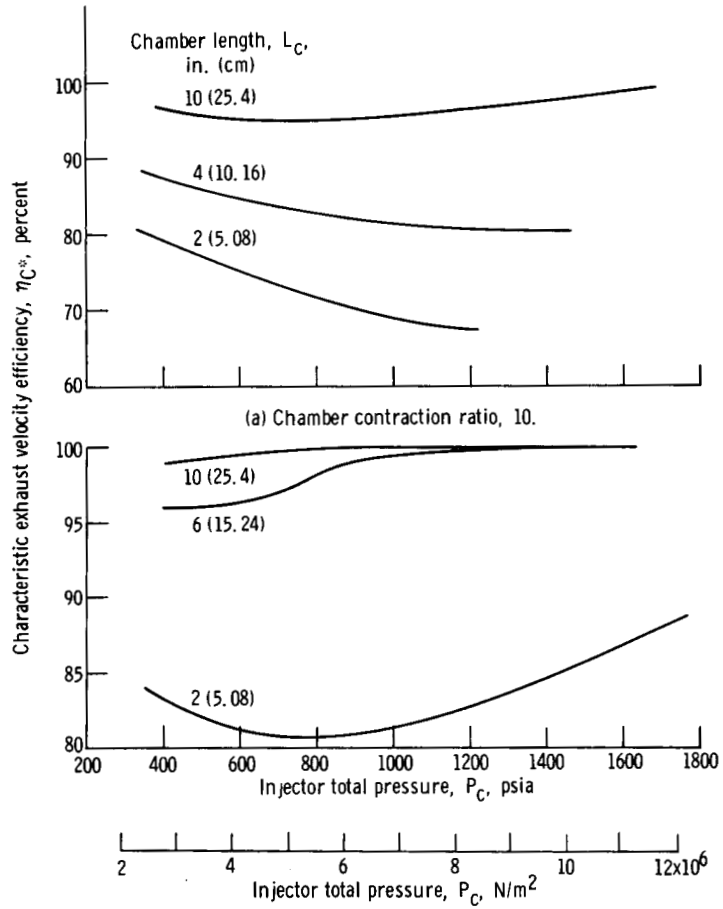

Figure 8. - Calculated characteristic exhaust velocity efficiency based on throat total pressure against injector total pressure.

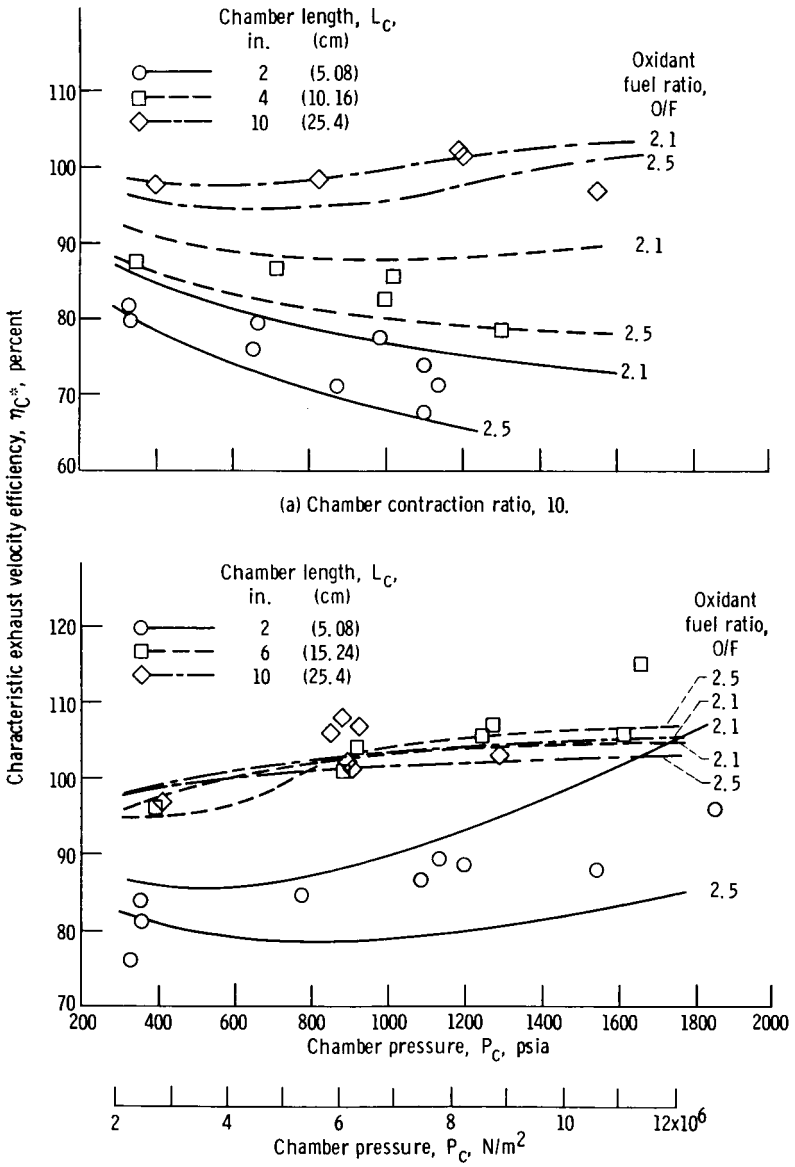

Figure 9. - Effect of oxidant-fuel ratio on calculated characteristic exhaust velocity efficiency.

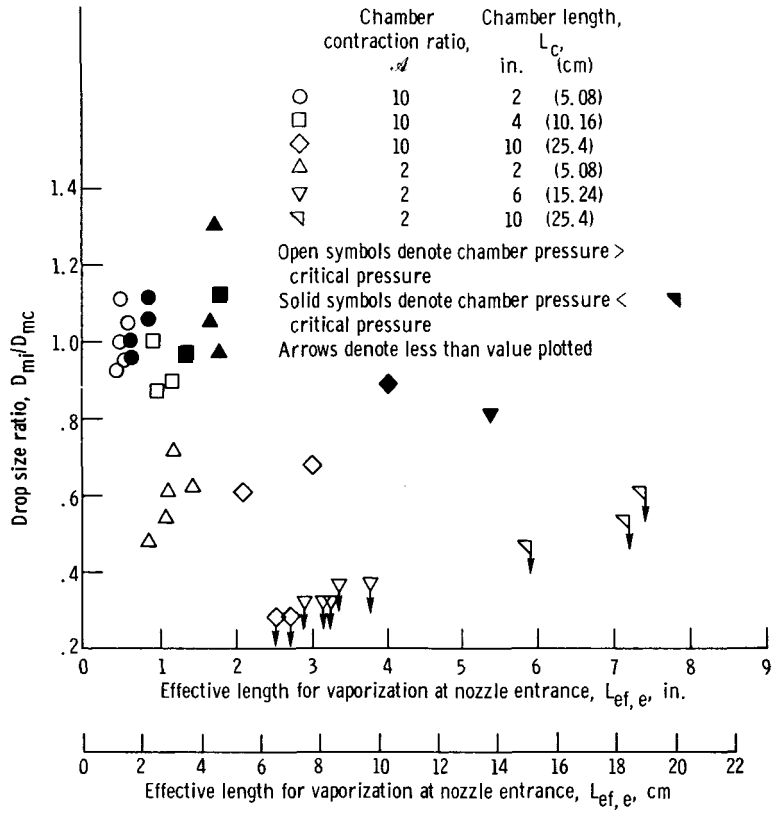

Figure 10. - Comparison of drop size necessary for vaporization model and correlated drop size.

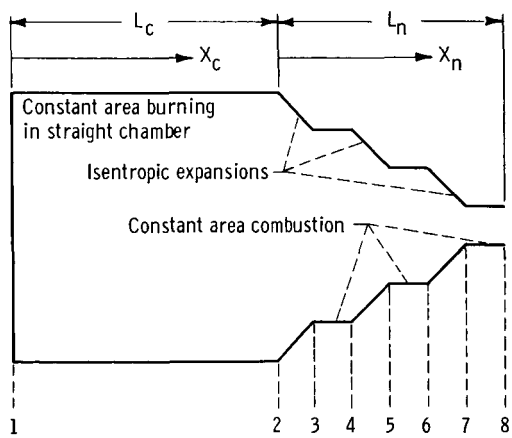

Figure 11. - Schematic of combustion model.

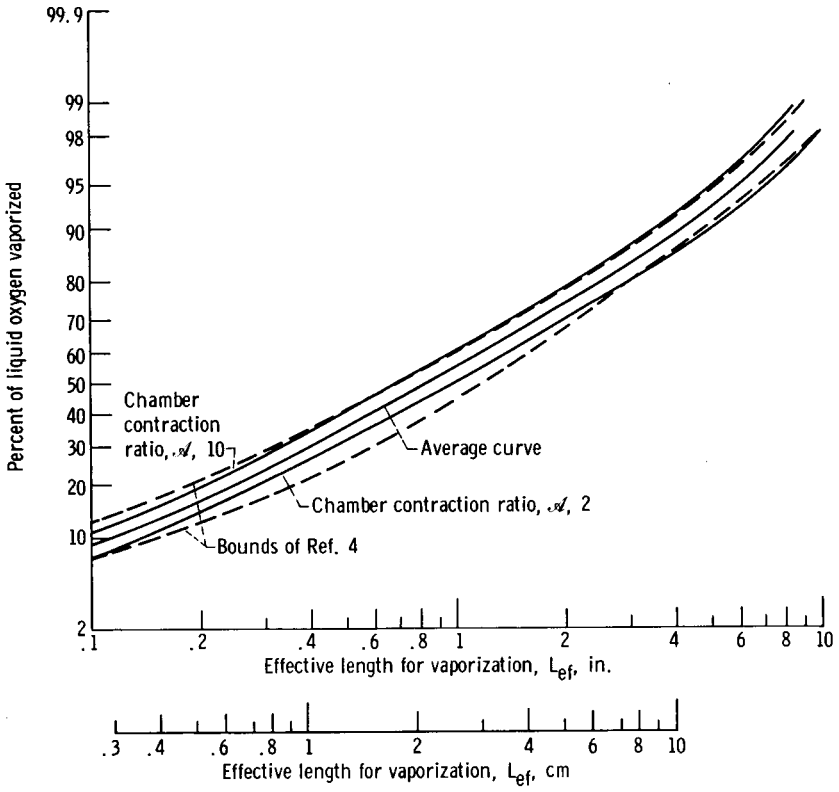

Figure 12. - Percent of liquid oxygen vaporized as function of effective length.

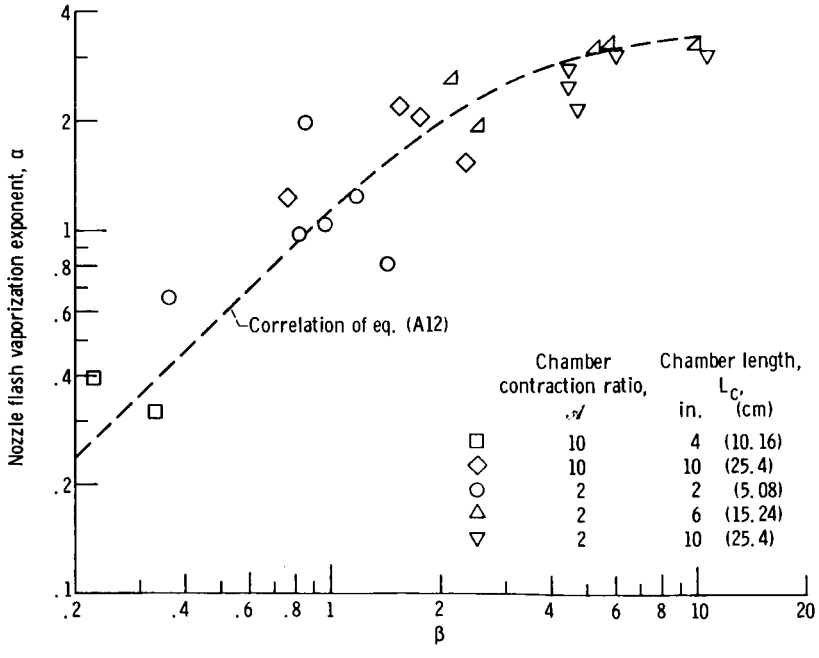

Figure 13. - Comparison of nozzle flash vaporization exponent with correlation for nozzle flash vaporization exponent.

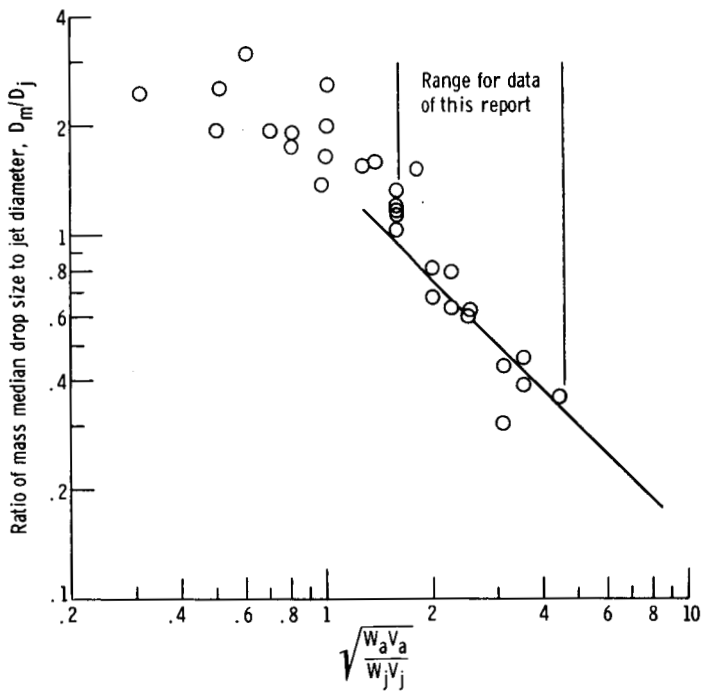

Figure 14. - Concentric-tube drop size correlation for water-air injector.